Materials Advances

ROYAL SOCIETY OF CHEMISTRY

PAPER

View Article Online
View Journal | View Issue

Cite this: *Mater. Adv.*, 2025, 6, 9709

Optimization of the carbonization temperature and composition of FeCC composites for enhanced lithium-ion battery anode performance

Do Thao Anh,[ab] Nguyen Bao Tran,[bc] Quang Ngoc Tran,[ab] Hanh Kieu Thi Ta,[abc] Bach Thang Phan,[abd] Tuan Loi Nguyen[ef] and Nhu Hoa Thi Tran *[bc]

Received 20th July 2025,
Accepted 21st October 2025

DOI: 10.1039/d5ma00782h

rsc.li/materials-advances

The collaboration between transition metal oxides (TMOs) and metal–organic framework (MOF) materials has become an effective strategy to enhance the electrochemical performance of lithium-ion batteries (LIBs). In this study, we focused on evaluating the impact of carbonization temperature and material mass ratios on the electrochemical performance of the anode electrode. Specifically, we combined Fe_3O_4 nanoparticles with a ZIF-67 rhombic dodecahedron (FZ67) through a simple and rapid chemical method. Subsequently, an Fe_3O_4@Co_3O_4/C (FeCC) hybrid composite structure was formed *via* one-step carbonization to develop an anode material. The survey of mass ratios and carbonization temperatures of the hybrid composite material showed their effect on the FeCC's structure and electrochemical performances. The results showed that the hybrid FeCC composite material structure can stabilize the anode electrode structure for LIBs by limiting the volume expansion of Fe_3O_4, shortening the lithium ion diffusion time, and improving the specific capacity compared to the anode electrode based-on ZIF-67. The electrochemical analysis results showed that at a current density of 0.1 A g^{-1}, the 0.3-FeCC-700 anode electrode maintained a storage capacity of 435 mAh g^{-1} after 80 cycles, with an efficiency that remained above 97%. Overall, the results of this study hold significant value for advancing anode materials in LIBs.

Introduction

Developing renewable energy sources has helped reduce environmental pollution and the depletion of fossil fuels on Earth. However, these natural energy sources have cumbersome energy conversion systems with high investment costs and cannot be used continuously or stored in devices like mobile phones, laptops, or electric vehicles.[1,2] Li-ion batteries (LIBs) are an innovative class of rechargeable batteries well-suited for use in electronic devices and hybrid vehicles. This is due to their eco-friendly nature, affordability, high energy storage capacity, safety, lack of memory effects, and long cycle life. These beneficial attributes make LIBs a prime choice for powering electronic gadgets and hybrid cars.[3] Graphite is a commonly used anode material in commercial LIBs; however, it exhibits low electrochemical performance, with a storage capacity of approximately 372 mAh g^{-1}, making it insufficient to meet the increasing energy storage demands.[4] Meanwhile, transition metal oxides (TMOs) are increasingly being studied because of several advantages, including high theoretical capacity, low cost, and abundant resources. As a member of the TMO group, Fe_3O_4 nanoparticles (Fe_3O_4 NPs) possess a higher theoretical capacity of 926 mAh g^{-1}, corresponding to 8 lithium ions per Fe_3O_4, rendering them a superior option compared to graphite anodes.[5] The reduction of Fe_3O_4 to Fe metal is an important electrochemical process in LIBs and involves two steps: the first step is the reduction of Fe_3O_4 by inserting lithium ions into $Li_xFe_3O_4$ nanoclusters. The insertion of lithium ions into $Li_xFe_3O_4$ can be described using eqn (1); the second step is the production of Fe metal, which can be described using eqn (2) or (3).[2]

$$Fe_3O_4 + xe^- + xLi^+ \rightarrow Li_xFe_3O_4 \qquad (1)$$

$$Li_xFe_3O_4 + (8 - x)Li^+ \rightarrow 4Li_2O + 3Fe^0 \qquad (2)$$

$$Fe_3O_4 + 8Li^+ + 8e^- \leftrightarrow 3Fe + 4Li_2O \qquad (3)$$

---

[a] Advanced Materials Technology Institute Vietnam National University Ho Chi Minh city (formerly affiliated with Center for Innovative Materials and Architectures), Ho Chi Minh City, Vietnam

[b] Viet Nam National University, Ho Chi Minh City, Vietnam. E-mail: ttnhoa@hcmus.edu.vn

[c] Faculty of Materials Science and Technology, University of Science, Ho Chi Minh City, Vietnam

[d] University of Health Sciences, Vietnam National University Ho Chi Minh City, Vietnam

[e] Institute of Fundamental and Applied Sciences, Duy Tan University, Ho Chi Minh City, Vietnam

[f] Faculty of Environmental and Chemical Engineering, Duy Tan University, Da Nang City, Vietnam

The Fe_3O_4 NPs have attracted considerable attention as a promising anode material for LIBs due to their high theoretical capacity, environmental friendliness, and ability to store multiple lithium ions per formula unit. Recent studies have highlighted the potential of Fe_3O_4-based composites as high-performance anode materials for LIBs through various structural and compositional modifications. Shi *et al.*[5] designed and synthesized an Fe_3O_4@CTP QD composite using coal tar pitch-derived quantum dots, which achieved a notable reversible capacity of 810 mAh g^{-1} over 200 cycles at 100 mA g^{-1} and maintained 547 mAh g^{-1} even at a high current density of 2000 mA g^{-1}, significantly outperforming pure Fe_3O_4. Kai Li *et al.*[6] reported three structures of Fe_3O_4@C composites featuring an octahedral morphology and a carbon coating and demonstrating remarkable capacities of 1063 mAh g^{-1} and 996 mAh g^{-1} at 0.5 and 1 A g^{-1}, respectively, after 300 cycles, indicating that the structural design plays a crucial role in enhancing electrochemical performance. Meanwhile, Zhuo Li *et al.*[7] reported variations of carbon-coated Fe_3O_4 electrodes, including Fe_3O_4@C-r, Fe_3O_4@C-d, and Fe_3O_4@C-s, which exhibited specific capacities of 990 mAh g^{-1}, 800 mAh g^{-1}, and 1180 mAh g^{-1}, respectively, after 100 cycles, demonstrating their strong cycling stability. Zhao *et al.*[8] prepared a SCNT/Fe_3O_4 nanocomposite, which integrated sulfonated carbon nanotubes, providing a stable framework for ion diffusion and delivering 674 mAh g^{-1} at 0.5 A g^{-1} after 100 cycles. In addition, other Fe-based active materials such as Fe_2O_3, when combined with carbon structures such as graphene and carbon nanotubes or doped with nitrogen, have also attracted considerable attention. For instance, cactus-like Fe_2O_3/C@NCNT hybrid micro–nano-structures delivered a high reversible capacity of 944.7 mAh g^{-1} after 600 cycles at 1 A g^{-1},[9] while Fe_3N/N-doped multilayer graphene (Fe_3N/N-mG) maintained a capacity of 530 mAh g^{-1} at 0.1 C after 600 cycles.[10] These advances highlight the synthesis of oxide–CNT/nitrogen-doped carbon composites as an emerging and significant design strategy for high-performance LIB anodes. Collectively, these studies affirm that combining metal oxide NPs based on Fe such as Fe_3O_4 NPs with conductive, porous carbon structures or engineered morphologies significantly boosts lithium storage capacity, rate performance, and long-term stability. However, despite significant advancements, the development of highly porous buffer frameworks that can effectively accommodate the volume expansion of Fe_3O_4 NPs during lithiation and delithiation remains a considerable challenge. Bridging this knowledge gap is crucial for optimizing material design strategies that enhance structural integrity, cycling stability, and overall lithium storage performance.

Zeolite imidazolate frameworks (ZIFs) are a class of metal–organic frameworks (MOFs) in which transition metal cations (M) are coordinated by bridging imidazole ligands, forming metal–imidazole–metal (M–Im–M) linkages within two-dimensional (2D) or three-dimensional (3D) frameworks. A cobalt-based zeolitic imidazolate framework (ZIF-67), which belongs to a subclass of MOFs consisting of Co^{2+} ions coordinated with nitrogen atoms of 2-methylimidazole to form a tetrahedral structural unit, has been chosen as a precursor to provide a stable carbon framework. The ZIF-67 material is particularly promising due to its unique structure, ease of synthesis, large surface area, tunable porosity, and excellent thermal and chemical stability.[11–13] Due to its low specific capacity and cycle performance, ZIF-67 and its derivatives are often used as sacrificial templates for the synthesis of various Co/C-based and Co_3O_4/C-based negative electrode materials or for designing special material structures to maximize the advantages of ZIF-67. For example, Jie Shao *et al.*[14] reported the synthesis of the ball-in-dodecahedron Co_3O_4 *via* two step pyrolysis of ZIF-67. The hollow dodecahedron morphology and efficient Li-storage *via* interfacial effects contribute to the outstanding Li-storage properties of this ZIF-67 derived Co_3O_4. This nanostructure demonstrated an exceptionally high reversible storage capacity of 1550 mAh g^{-1} and retained a substantial storage capacity of 1335 mAh g^{-1} after 100 cycles, indicative of excellent cycling stability. Mingxuan Guo *et al.*[15] presented hybrid porous carbons with a high initial capacity of 677 mAh g^{-1} at 50 mA g^{-1}, which could be maintained at 312 mAh g^{-1} after 100 cycles. Recently, Wang *et al.*[13] reported the Si@NC-ZIF structure, derived from ZIF-67, demonstrating outstanding capacity retention and maintaining 1623.05 mAh g^{-1} after 100 cycles at 200 mA g^{-1}, with a retention rate of 86.29%. Meanwhile, the one-dimensional CoSe@NC-550 nanofibers reported by Liu *et al.*[16] exhibit excellent storage characteristics, delivering a high capacity of 796 mAh g^{-1} at a current of 1 A g^{-1} for 100 cycles. Overall, ZIF-67 exhibits great potential for extensive research in the fields of energy storage materials in general and anode materials for lithium batteries in particular. Besides, the effects of carbonization temperature and weight distribution between hybrid composite components on battery performance should be specifically addressed to establish a more straightforward approach for future studies.

Herein, we propose a novel composite material design strategy, in which Fe_3O_4 NPs are combined with a ZIF-67 framework to form a hybrid composite material called FeCC. Under appropriate thermal treatment conditions, ZIF-67 decomposes to form a conductive carbon network that surrounds and anchors the Fe_3O_4 NPs, resulting in a synergistic composite structure. In this structure, Fe_3O_4 NPs serve as a high-capacity component, while the porous carbon framework derived from ZIF-67 enhances electrical conductivity, stabilizes the structure, alleviates mechanical stress during cycling, and contributes to the formation of a more stable solid electrolyte interphase (SEI) film. These results demonstrated the primary importance of modulating the composition ratios of structures for the design of future energy storage materials.

Experimental

Synthetic procedures

Preparation of ZIF-67. A ZIF-67 rhombic dodecahedron structure was synthesized based on the previously reported literature with minor modifications.[17,18] A mixed solution containing 116 mg of cobaltous nitrate, 131 mg of Hmim, and 137.5 mg of PVP in methanol was prepared and stirred magnetically for 24 hours at room temperature. The solution appeared purple, and the nanoparticles were separated from the dispersion by centrifugation at 4500 rpm, followed by washing with methanol. The material was then dried overnight in a vacuum oven at 80 °C.

Preparation of Fe_3O_4 NPs. In a typical process reported by Phuc *et al.*,[19] the Fe_3O_4 NPs were prepared by using 1982 mg of ferric chloride hexahydrate and 1731 mg of ferrous chloride tetrahydrate in 50 mL of DI water, forming solution A. Solution B consisted of 2437 mg of sodium citrate in 9 mL of DI water. Meanwhile, 12 mL of ammonium hydroxide solution was also prepared. First, solution A in a flask was stirred continuously until the reaction temperature reached 80 °C. Then, solution B and ammonium hydroxide solution were dripped simultaneously for 30 minutes. A black precipitate formed. The particles were separated magnetically and thoroughly washed multiple times with deionized water and ethanol. The entire reaction process had to be carried out in a N_2 gas atmosphere combined with continuous stirring.

Preparation of a FeCC hybrid composite. The hybrid composite material was synthesized by mixing a given amount of pre-synthesized Fe_3O_4 NPs, 51.721 of mg cobaltous nitrate, 39.682 mg of Hmim and 2784 mg of PVP in 80 mL of methanolic solution by mechanical stirring for 24 hours. The purple sediment was repeatedly washed with methanol by centrifuging at 4500 rpm for 5 minutes each time, followed by drying under a vacuum. The obtained samples were denoted as *x*-FZ67 (x = 0.2 g, 0.3 g and 0.4 g), where x refers to the weight of as-prepared Fe_3O_4, respectively. The *x*-FZ67 samples were directly carbonized in a tube furnace for 2.5 hours at a heating rate of 5 °C min^{-1} in a N_2 atmosphere. The samples obtained were conventionally denoted as *x*-FeCC-*y* (y = 100 °C, 400 °C and 700 °C), where y refers to the carbonization temperature. The formation of the FeCC hybrid composite material is described in Scheme 1.

Electrode fabrication and electrochemical measurements

The anode was prepared by coating a slurry mixture onto a copper foil current collector. The slurry consisted of 70 wt% active material, 15 wt% PVDF binder, and 15 wt% Super P conductive additive, all dispersed in NMP solvent. To eliminate potential bubble formation, the coated electrodes were vacuum-dried at 120 °C for 6 hours before electrochemical testing. Circular anodic disks with a diameter of 15 mm were then punched from the dried film, achieving an active material loading of approximately 1.5–2.0 mg cm^{-2}. CR2032-type coin cells were assembled in an argon-filled glovebox, utilizing lithium metal as the counter electrode and a polypropylene (Celgard 2400) membrane as the separator. The electrolyte solution comprised 1.0 M lithium hexafluorophosphate ($LiPF_6$) dissolved in a 1 : 1 (v/v) mixture of ethylene carbonate and diethyl carbonate.

Results and discussion

The structures and the crystal phases of the synthesized Fe_3O_4, ZIF-67, and *x*-FZ67 obtained using XRD are indicated in Fig. 1a. The Fe_3O_4 NPs exhibited diffraction peaks corresponding to the (220), (311), (400), (422), (511), and (440) crystal planes.[5] Meanwhile, the observed diffraction peaks of the synthesized ZIF-67 material corresponded to the (011), (002), (112), (222), and (134) crystallographic planes of ZIF-67, respectively.[20] For the 0.2-FZ67, 0.3-FZ67 and 0.4-FZ67 samples, the appearance of diffraction peaks in the patterns corresponded to the crystal structures of ZIF-67 and Fe_3O_4. The excellent agreement between the measured diffraction peaks and known crystal facets provides evidence that Fe_3O_4, ZIF-67 and *x*-FZ67 were successfully synthesized with the anticipated crystal orientation. The crystal structures of *x*-FeCC-*y* after carbonization are shown in Fig. 1b; the characteristic peaks at diffraction angles 2θ of 18.4°, 30.4°, 35.7°, 43.4°, 53.8°, 57.3°, and 63.1° corresponded to the (111), (220), (311), (400), (422), (511), and (440)

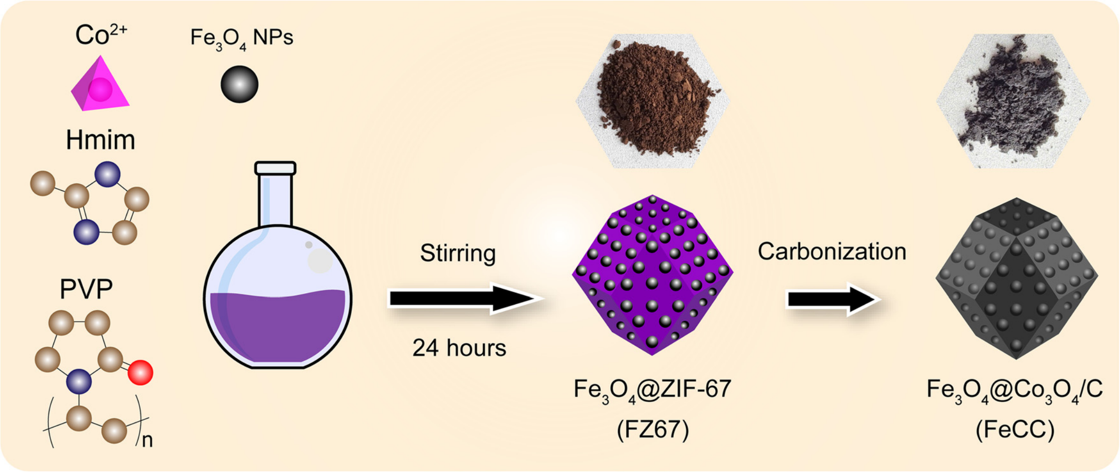

Scheme 1 Synthetic procedure of the FeCC hybrid composite.

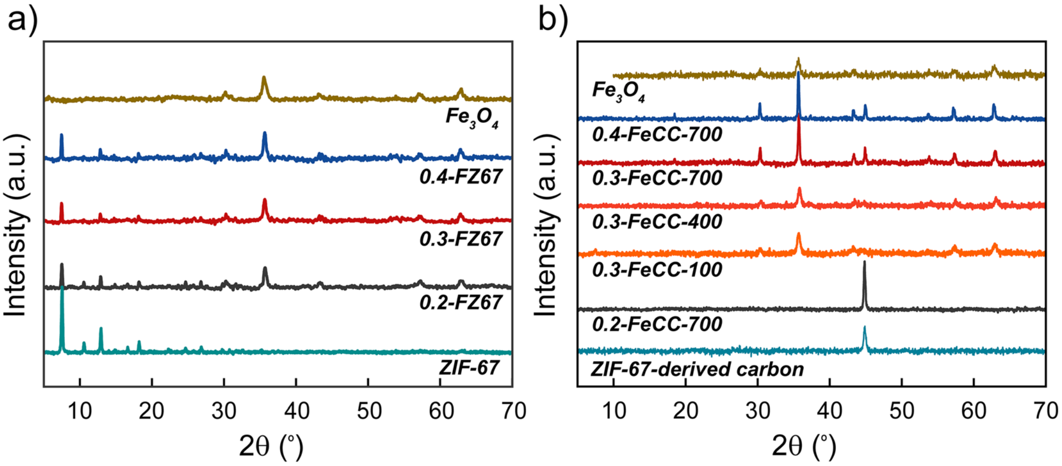

Fig. 1 (a) XRD patterns of (a) Fe_3O_4 NPs, ZIF-67, *x*-FZ67 and (b) Fe_3O_4 NPs, ZIF-67-derived carbon and *x*-FeCC-*y*.

crystallographic planes of the Fe_3O_4 NP structure.[5] Meanwhile, the diffraction peaks occurring at 44.9° in the XRD pattern of FeCC carbonization at 700 °C corresponded to (400) crystal planes of Co_3O_4 (JCPDS #43-1003).[21] In the report of Weihai *et al.*,[22] it was shown that during the carbonization of the ZIF-67 precursor, Co^{2+} could not only be reduced directly to metallic Co but also could be partially incorporated by the O element inside materials to form cobalt oxides such as Co_3O_4.

The vibrations of chemical bonds in Fe_3O_4 NPs, ZIF-67, and *x*-FeCC-700 hybrid composites were analyzed in the FTIR spectra. As shown in Fig. S1 (SI), Fe_3O_4 NPs displayed a vibrational band at 590 cm^{-1}, corresponding to the Fe–O stretching vibration of Fe_3O_4. A strong infrared peak appeared at 1629 cm^{-1}, corresponding to the bending vibration of hydroxyl groups.[19] Meanwhile, the vibrational peak at 1373 cm^{-1} was identified as the characteristic peak of $-NH_3$ formed during the synthesis of Fe_3O_4 NPs.[23] On the other hand, the FTIR spectrum of ZIF-67 displayed a Co–N stretching vibration at 424 cm^{-1}, while characteristic peaks within the range of 1500–800 cm^{-1} and below 800 cm^{-1} were assigned to the vibrational modes of the imidazole ring from Hmim ligands. Peaks at 2922 cm^{-1} and 3134 cm^{-1} corresponded to the C–H stretching vibrations in the aromatic ring and aliphatic chains of the bridging structure in ZIF-67. Additionally, the O–H and N–H vibrational bands of Hmim were observed around 3400 cm^{-1}.[24–26] When comparing the FTIR spectra of the *x*-FeCC-700 samples with that of Fe_3O_4, the Fe–O vibrations and hydroxyl groups remained present. However, in comparison with ZIF-67, the characteristic imidazole peaks within the range of 800–1500 cm^{-1} were either significantly weakened or completely disappeared, indicating the decomposition of the imidazole structure during the carbonization process. This was consistent with the formation of Fe_3O_4 NPs and ZIF-67-devired carbon during pyrolysis. In addition, the morphology of the Fe_3O_4 NPs and ZIF-67 template is shown in Fig. S2 (SI). The Fe_3O_4 NPs (Fig. S2a) presented uniform nanospheres with a diameter of approximately 30 nm. Meanwhile, the ZIF-67 precursor (Fig. S2b) showed a rhombic dodecahedron structure, with the diameter ranging from 150 to 250 nm and featuring a smooth surface, consistent with previous reports in the literature.[27,28] As shown in Fig. S3 (SISI), the 0.3-FeCC-100 and 0.3-FeCC-400 samples maintained the morphology of ZIF-67 and showed no significant difference compared to 0.3-FZ67 (Fig. 2b), indicating that within this temperature range, the sintering effect was not strong enough to cause significant aggregation. In contrast, the 0.3-FeCC-700 sample (Fig. 2e) exhibited intense aggregation and an increase in the material size due to the accelerated diffusion at high temperatures. This allowed the particles to move closer together, while the dehydration or decomposition of organic bonds in ZIF-67 contributed to structural changes. Additionally, the degree of deformation caused by sintering was influenced by the ratio of the two material components. Specifically, the 0.2-FeCC-700 sample (Fig. 2d) failed to retain its rhombic polyhedral shape due to its lowest Fe_3O_4 content, leading to poorer thermal stability and making the material more prone to breakdown at high temperatures. In contrast, the 0.4-FeCC-700 sample (Fig. 2f) preserved its polyhedral morphology with well-defined grain boundaries, as its higher Fe_3O_4 content enhanced thermal stability and mitigated excessive sintering.

The FESEM-EDS elemental mapping results and EDS pattern of 0.3-FeCC-700 are given in Fig. 3(a and b). It is seen that the Co, Fe, O, N and C elements were homogeneously distributed on the surface of the sample. The atomic ratio of the elements is presented in the inset table in Fig. 3b and Fe-content of the sample was the highest among the others and element O comes second because O was present in the composition of Fe_3O_4 and Co_3O_4. The ratios of Co and N elements are very close to each other while C was the lowest. In the HRTEM image of 0.3-FeCC-700 in Fig. 3(c and d), the *d*-spacing of 0.26 nm was assigned to the (311) facet of Fe_3O_4, while the 0.34 nm spacing was consistent with the (002) lattice planes of graphite.[29] As revealed in Fig. 3d, a clear lattice with a lattice spacing of 0.26 nm corresponded to the (311) lattice of Fe_3O_4.[30] Meanwhile lattice distances were 0.24 nm and 0.278 nm, which corresponded to the (311) and (220) crystal planes of Co_3O_4.[31]

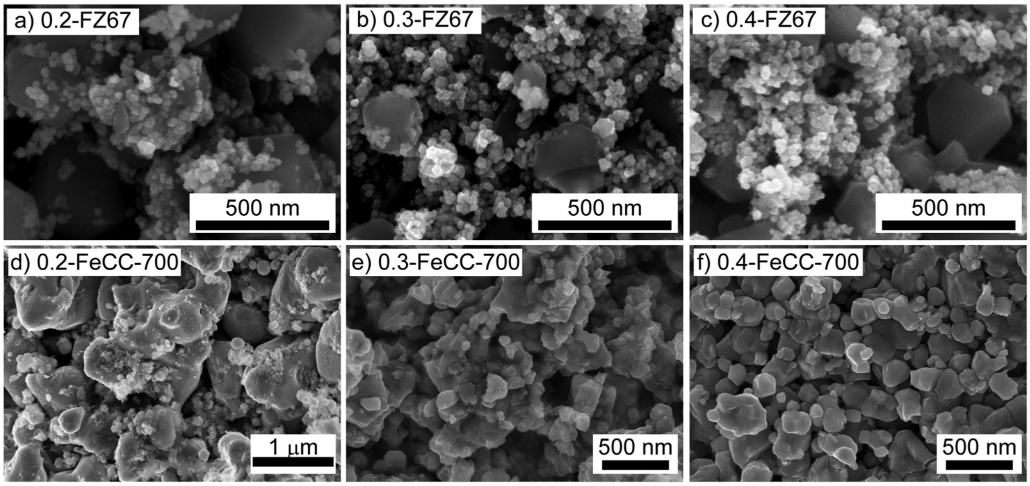

Fig. 2 FESEM images of (a)–(c) *x*-FZ67 and (d)–(f) *x*-FeCC-*y* hybrid composite structures.

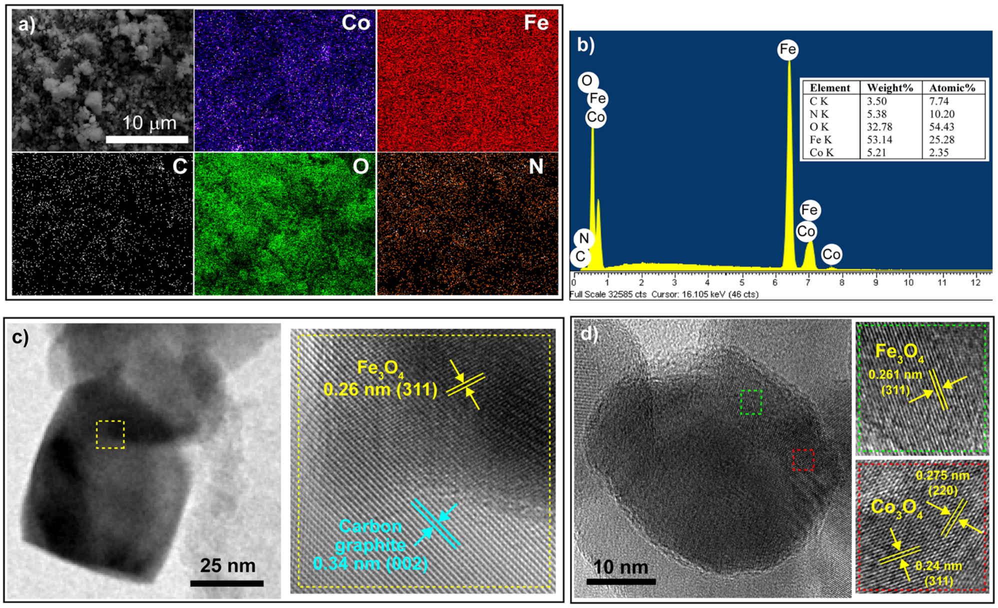

Element	Weight%	Atomic%
C K	3.50	7.74
N K	5.38	10.20
O K	32.78	54.43
Fe K	53.14	25.28
Co K	5.21	2.35

Fig. 3 (a) FESEM-EDS elemental mapping; (b) EDS pattern, and (c) and (d) HRTEM image of the 0.3-FeCC-700 hybrid composite.

These results were consistent with the EDS mapping and EDS pattern results shown in Fig. 3(a and b), providing strong evidence for the coexistence of Fe_3O_4, Co_3O_4, and graphite phases.

The XPS survey spectrum of the material is shown in Fig. 4a; four characteristic peaks of Co 2p, Fe 2p, O 1s and C 1s were presented.[32] The binding energy of Co 2p shown in Fig. 4b consists of Co $2p_{3/2}$ and Co $2p_{1/2}$ at 781.58 eV and 796.08 eV, respectively, representing the maximum positions of Co^{2+}. The energy levels at 779.68 eV and 795.18 eV corresponded to the peaks of Co^{3+}. Additionally, the Co 2p spectrum exhibits two satellite peaks at 786.08 eV and 802.78 eV, which have been assigned to the vibrations of Co^{2+}. The high-resolution XPS spectrum of Fe 2p illustrated in Fig. 4c shows two distinct spectral bands situated at 723.88 eV and 712.68 eV, attributed to the Fe $2p_{1/2}$ and Fe $2p_{3/2}$ spin–orbit splits of Fe^{3+} species, respectively. Additionally, two ancillary peaks were observed at binding energies of 726.38 eV and 710.28 eV, which can be ascribed to the Fe $2p_{1/2}$ and Fe $2p_{3/2}$ transitions of Fe^{2+} species. Furthermore, two minor satellite peaks were discerned at 718.88 eV and 732.78 eV, corresponding to the vibrational shake-up transitions associated with Fe^{2+} ions.[33,34] In Fig. 4d, the spectrum of O 1s resolved into two peaks at 529.68 eV, showing the binding of Co–O and Fe–O; the binding energy of 531.2 eV corresponded to H–O.[34,35] Not shown in the full survey spectrum, the N 1s high-resolution spectrum in Fig. 4e of 0.3-FeCC-700 showed that there were mainly three types of nitrogen species: pyridinic-N (N–H) at 398.01 eV, pyrrolic-N (N–C) at

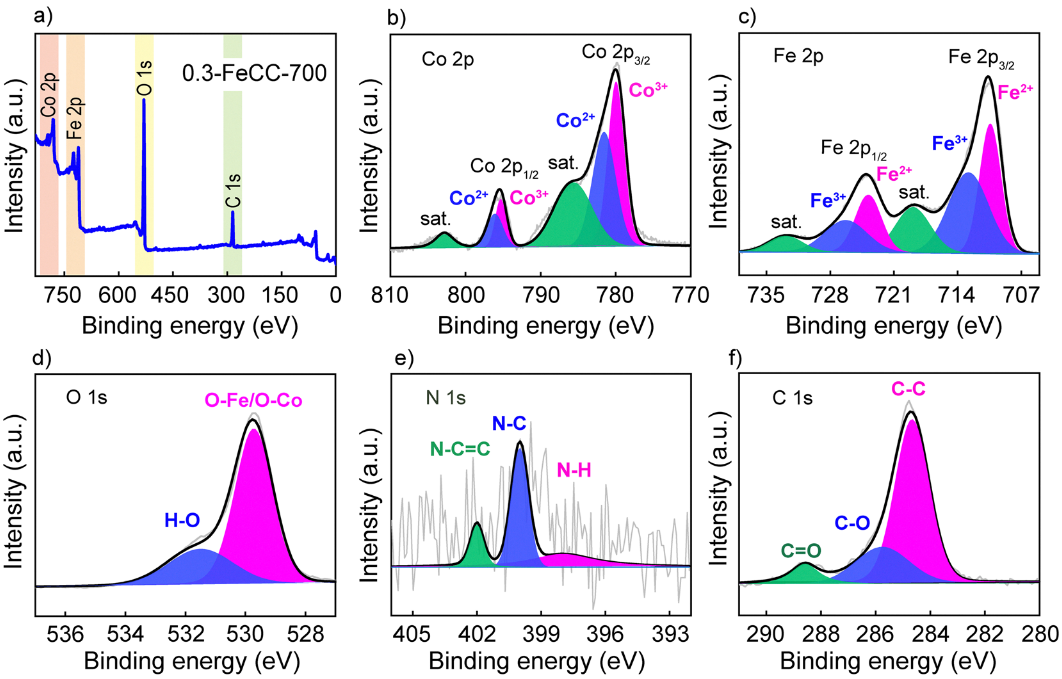

Fig. 4 XPS spectra of 0.3-FeCC-700 hybrid composites: (a) survey scan, and high-resolution spectra of (b) Co 2p, (c) Fe 2p, (d) O 1s, (e) N 1s, and (f) C 1s.

400.05 eV, and graphitic-N (N–C=C) at 402.05 eV.[36,37] Ming Zhong *et al.*[38] reported that high temperature could reduce the amount of heteroatoms such as N, S, P, *etc.*, which were typical active sites for the fast kinetics of electrochemical reactions. This may explain why the N 1s configuration did not appear in the full survey spectrum of 0.3-FeCC-700. Finally, the high-resolution C 1s spectrum in Fig. 4f reveals three distinct carbon bond types at 284.8 eV, 285.82 eV, and 288.57 eV, which are attributed to C–C, C–O, and C=O bonds, respectively.[39,40]

The electrochemical performance of Fe_3O_4 and ZIF-67-derived carbon anode electrodes in LIBs was evaluated using galvanostatic charge/discharge (GCD) curves and coulombic efficiency (CE) at 0.1 A g^{-1}. The Fe_3O_4 anode electrode delivered high initial charge and discharge capacities of 984 and 1298 mAh g^{-1}, respectively, with an initial coulombic efficiency (ICE) of 76%. This low efficiency was attributed to the formation of the solid electrolyte interphase (SEI) film and the stepwise reduction of Fe_3O_4 to Fe. In contrast, the ZIF-67-derived carbon electrode showed lower initial charge and discharge capacities of 438 and 901 mAh g^{-1}, respectively, and an ICE of 49%, likely due to significant irreversible electrolyte decomposition. Although Fe_3O_4 exceeded its theoretical capacity, rapid fading occurred after ∼20 cycles. Meanwhile, the ZIF-67-derived carbon maintained 191.9 mAh g^{-1} after 100 cycles with nearly 100% CE, highlighting its superior cycling stability despite a lower initial capacity. The GCD curves of the first cycle and the CEs of the 0.2-FeCC-700, 0.3-FeCC-100, 0.3-FeCC-400, 0.3-FeCC-700, 0.4-FeCC-100, 0.4-FeCC-400, and 0.4-FeCC-700 anode electrodes are presented in Fig. 5 and Table 1.

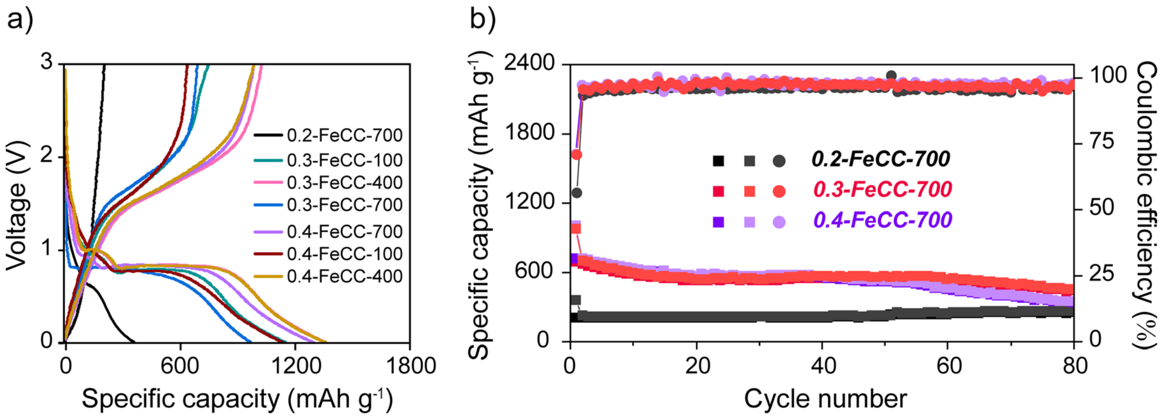

Fig. 5 (a) Galvanostatic charge/discharge curves at the first cycle of *x*-FeCC-*y* anode electrodes and (b) coulombic efficiency of *x*-FeCC-700 anode electrodes.

Table 1 discharge/charge capacities and CEs of anode electrodes at the first cycle

Anode electrode	Discharge capacity (mAh g^{-1})	Charge capacity (mAh g^{-1})	CE (%)
0.2-FeCC-700	358	202	56
0.3-FeCC-100	1150	746	65
0.3-FeCC-400	1361	1024	75
0.3-FeCC-700	970	688	71
0.4-FeCC-100	1361	985	72
0.4-FeCC-400	1138	636	88
0.4-FeCC-700	1006	715	71

In Fig. 5a, during the initial discharge of all the anode electrodes, a distinct and extended voltage plateau was observed between 0.6 V and 1.0 V, which is primarily attributed to the conversion reaction between Fe_3O_4 and lithium ions. This voltage range also corresponds to the formation and partial decomposition of the SEI film, resulting from the reductive decomposition of electrolyte components on the electrode surface. The notable gap between the initial discharge and charge capacities, along with the low initial CE, further confirms SEI film formation in all samples. The carbonization temperature of the active material has a profound impact on the electrochemical performance of LIBs, as it governs the final morphology, composition, surface area, and porosity of MOF-derived composites. At higher pyrolysis temperatures, the organic ligands of the MOF decompose more completely, promoting the formation of a more ordered graphitic carbon framework with improved electrical conductivity. However, excessively high temperatures may lead to partial or complete collapse of the original porous structure of the MOF and simultaneously reduce the content of heteroatoms (*e.g.*, N, S, and P),[38] which are known to provide additional active sites and facilitate fast electrochemical reaction kinetics. In the case of the 0.3-FeCC-100 (Fig. S5b), 0.3-FeCC-400 (Fig. S5c), 0.4-FeCC-400 (Fig. S5e) and 0.4-FeCC-400 (Fig. S5f) samples, the relatively low carbonization temperatures result in incomplete decomposition of the MOF precursor, leaving behind residual organic moieties and heteroatoms such as N. While these structural features contribute to the initially high discharge capacities, they also render the electrodes structurally unstable, since a well-ordered graphitic carbon framework has not yet been established. Therefore, these samples suffered rapid structural degradation during cycling, which was evidenced by the rapid capacity loss observed in the first three-cycle GCD curves (Fig. S5) and CE (Fig. S5h). In contrast, the 0.3-FeCC-700 and 0.4-FeCC-700 electrodes achieve a more favorable balance. The higher carbonization temperature promotes the decomposition of organic ligands and the formation of a more ordered graphitic carbon framework, which improves electrical conductivity and structural robustness. Consequently, these electrodes maintain distinct redox features and stable capacity retention over extended cycling. On the other hand, the 0.2-FeCC-700 electrode exhibits significantly lower recovered capacity, approximately three times less than that of 0.3-FeCC-700 and 0.4-FeCC-700, reflecting its limited Li^+ ion storage capacity.

The differential capacity (d*Q*/d*V*) curves in Fig. S6 provide direct insights into the redox behaviors of the electrodes during cycling. For the 0.2-FeCC-700 sample, the anodic and cathodic peaks remain clearly visible even after 60 cycles, with negligible peak shift and minimal loss of intensity, suggesting highly reversible redox reactions and excellent structural stability. Similarly, both 0.3-FeCC-700 and 0.4-FeCC-700 retain distinguishable anodic/cathodic peaks at the 60th cycle, although with reduced intensity compared to the first cycle, indicating that while the redox kinetics slow down, the conversion reactions remain partially reversible. In contrast, the electrodes carbonized at lower temperatures, including 0.3-FeCC-100, 0.3-FeCC-400, 0.4-FeCC-100, and 0.4-FeCC-400, almost completely lose their anodic and cathodic peaks after 60 cycles. Moreover, in the differential capacity curves, the noticeable peak shift accompanied by peak fading suggests an increase in internal resistance and polarization, leading to suppressed lithiation/delithiation reversibility. This behavior can be attributed to structural degradation, particle aggregation, and poor electrical conductivity. Overall, the results demonstrate that 700 °C temperature carbonization significantly improves the structural robustness and redox reversibility of the electrodes, allowing them to maintain well-defined redox peaks over prolonged cycling, whereas lower-temperature treated samples rapidly lose their redox activity.

Although the 0.2-FeCC-700 anode exhibited a high CE (Fig. 5b), attributed to the encapsulation of Fe_3O_4 NPs within the ZIF-67-derived carbon framework, its specific capacity remained relatively low at approximately 256/248 mAh g^{-1} with a CE of 97% after 80 cycles. Meanwhile, the 0.4-FeCC-700 anode achieved a specific capacity of 344/338 mAh g^{-1} and a CE of 98% after 80 cycles (Fig. 5b). These variations in specific capacity were primarily influenced by differences in the quantity of iron ions, which play a crucial role as electron transport mediators within the electrode structure. According to Yan *et al.*,[33] strong chemical bonding between Fe_3O_4 and the carbon matrix prevents nanoparticle agglomeration, while the porous carbon coating accommodates volume changes of Fe_3O_4 during charge/discharge cycles. However, when the concentration of Fe_3O_4 exceeded the optimal equilibrium level, the stability of the *x*-FeCC-700 hybrid composite deteriorated over prolonged cycling. This instability was reflected in the capacity decline observed around the 40th cycle for the 0.4-FeCC-700 anode. Consequently, the optimized structure and composition of the 0.3-FeCC-700 anode contributed to its superior electrochemical performance. In addition, when compared with some anode electrodes based solely on Fe or MOFs (Table S1), the 0.3-FeCC-700 anode electrode also demonstrated superior performance. Overall, the GCD analysis highlights that while SEI film formation accounts for the high initial capacity of all electrodes, only the 700 °C-treated samples, including 0.3-FeCC-700 and 0.4-FeCC-700, provide a stable conductive framework capable of sustaining long-term cycling.

The CV curves recorded for 0.3-FeCC-700 and 0.4-FeCC-700 electrodes indicate the specific electrochemical processes of lithiation and delithiation during the first three cycles.

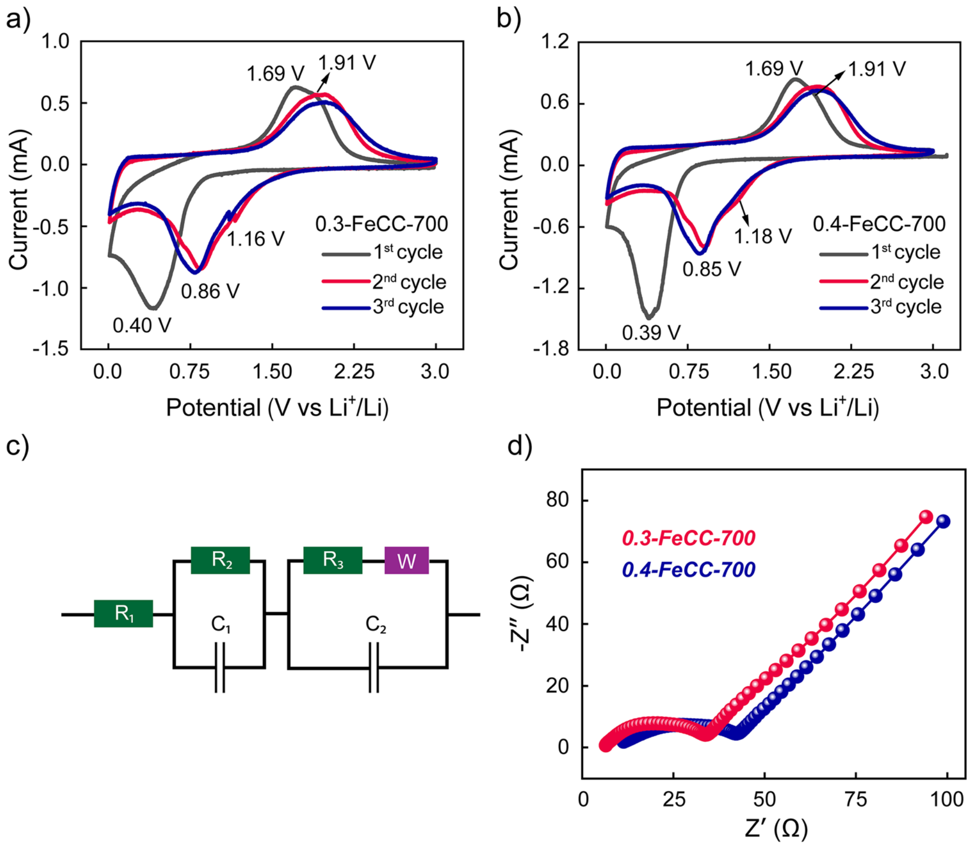

Fig. 6 (a)–(b) CV curves at a scan rate of 0.3 mV s^{-1}; (c) equivalent circuit model for EIS data fitting and (d) EIS spectra of 0.3-FeCC-700 and 0.4-FeCC-700 electrodes at the frequency ranging from 100 kHz to 100 mHz.

Measurements were conducted at a scan rate of 0.3 mV s^{-1} within the voltage range of 0.01–3.0 V, as shown in Fig. 6(a and b). In the first cathodic scan, a broad peak centered at approximately 0.4 V for the 0.3-FeCC-700 sample and 0.39 V for the 0.4-FeCC-700 sample was observed, corresponding to the conversion reaction of Fe_3O_4 with lithium ions to form metallic Fe and Li_2O, corresponding to eqn (1), (2), and (3),[2] as well as the formation of the SEI film through the reductive decomposition of the electrolyte.[41,42] Furthermore, a relatively low-potential peak at 0.01 V was observed, which can be attributed to the Li^+ intercalation into the carbon component of the FeCC composite. In a study conducted by González-Banciella *et al.*,[43] it was observed that the formation of the SEI film occurred at distinct voltage regions depending on the nature of the active material. Specifically, SEI film formation at the carbon fiber/electrolyte interface was indicated by a broad cathodic peak near 0 V, whereas SEI film formation at the TMO/electrolyte interface occurred near 0.7 V. Moreover, the overlap and stabilization of redox peaks associated with $Fe^{3+}/Fe^{2+}/Fe^0$ in subsequent cycles were interpreted as signs of SEI film completion and improved electrode reversibility. During the initial anodic scan, broad peaks appearing around 1.69 V and 1.91 V can be attributed to the oxidation of Fe^0 to Fe^{2+} and Fe^0 to Fe^{3+}, respectively, as described in eqn (3).[2] In this experiment, the characteristic anodic peaks of Co_3O_4 may overlap with those of Fe_3O_4 due to their close potential values. According to Liming Chen *et al.*,[2,44] the oxidation peak of Co_3O_4 appears at 1.95 V, which is very close to the Fe_3O_4 oxidation region. However, Jie Chen *et al.* previously reported the oxidation peak at 2.12 V corresponding to the oxidation of Co to Co_3O_4, suggesting an ~2 V shift in the peak position.[45] Given that Fe_3O_4 is the dominant phase in the composite, the anodic peaks of Fe_3O_4 exhibit a greater intensity and area than those of Co_3O_4, making the latter difficult to distinguish. The overall redox reactions of Co_3O_4 during cycling are described in eqn (4) and (5).[46] Notably, in the second and third cycles, the cathodic peaks shift slightly and become sharper, while the initial SEI-related peak at 0.01 V diminishes, further supporting the formation of a stable SEI and the improved reversibility of redox reactions. These results demonstrate that the FeCC composite structure effectively accommodates the volume changes associated with conversion reactions and facilitates stable lithium-ion transport during cycling.

$$CoO + 2Li^+ + 2e^- \leftrightarrow Co + Li_2O \tag{4}$$

$$Co_3O_4 + 8Li^+ + 8e^- \leftrightarrow 3Co + 4Li_2O \tag{5}$$

However, it should be noted that the material composition analysis results in Fig. 3b indicate that cobalt accounts for only a very small proportion. Therefore, the actual active sites of the

FeCC electrode material are primarily attributed to Fe_3O_4, which dominates the electrochemical reactions described in eqn (1)–(3).

The EIS was conducted on the 0.3-FeCC-700 and 0.4-FeCC-700 anode electrode to examine the kinetic and mechanical data of both electrochemical systems (Fig. 6(c and d)). Nyquist plots showed a single semicircle, representing the electrode/electrolyte interfacial resistance. Herein, R_1 refers to the Ohmic resistance from the electrolyte; R_2 is the SEI film resistance; R_3 represents the charge-transfer resistance; and W denotes the Warburg impedance. C_1 and C_2 represent the corresponding capacitance values.[47] The difference in electrochemical performance between 0.3-FeCC-700 and 0.4-FeCC-700 originates from the variation in material composition. While the ZIF-67 content remained constant, the Fe_3O_4 content was adjusted, leading to differences in the amount of Fe_3O_4 formed after heat treatment. The 0.4-FeCC-700 sample contained a higher amount of Fe_3O_4 compared to 0.3-FeCC-700, which affected the cycling stability of the material. Previous studies, as well as this research, have shown that although Fe_3O_4 possesses high capacity, it tends to aggregate and degrade during cycling, leading to performance deterioration. Therefore, ZIF-67 was used as a sacrificial precursor to form a carbon framework that encapsulates Fe_3O_4, helping to mitigate volume expansion during electrochemical cycling. However, with a higher Fe_3O_4 content, the Fe_3O_4 NPs in 0.4-FeCC-700 may not have been fully encapsulated by the carbon matrix, reducing structural stability. Additionally, the SEI film formed on the electrode surface plays a crucial role in protecting the material. Although the SEI results in unwanted side reactions, it provides lithium-ion conductivity and electronic insulation, preventing continuous electrolyte decomposition and thus preserving anode kinetics. The R_1, R_2, and R_3 values of the 0.3-FeCC-700 electrode are 7.086 Ω, 7.103 Ω, and 15.16 Ω, respectively, while those of the 0.4-FeCC-700 electrode are 12.38 Ω, 8.642 Ω, and 15.76 Ω. The EIS results indicate that the R_2 value of 0.3-FeCC-700 is lower than that of 0.4-FeCC-700, and the smaller semicircle in the Nyquist plot of 0.3-FeCC-700 (Fig. 6d) suggests a lower overall impedance. This implies that the SEI film on the 0.3-FeCC-700 electrode is stable and supports efficient charge transfer with minimal resistance. In contrast, the EIS data for the 0.4-FeCC-700 electrode suggest a breakdown of the native passivating film during lithium plating/stripping, exposing fresh surfaces of the active material to the electrolyte. This repeated exposure promotes dead lithium formation and continuous electrolyte consumption, increasing the SEI surface area and accelerating electrolyte depletion during battery operation. In summary, the difference in material ratios, or, in other words, the better encapsulation of Fe_3O_4 NPs by carbon derived from ZIF-67 made the 0.3-FeCC-700 composite more structurally suitable as an anode electrode for LIBs.

The kinetic analysis of the 0.3-FeCC-700 and 0.4-FeCC-700 anodes in LIBs was performed through investigating CV curves at scan rates of 0.3 to 1.2 mV s^{-1} and over a voltage window of 0.01 to 3.00 V, as shown Fig. 7(a and b). The results of the pseudo-capacitance contribution and diffusion control contribution based on the CV curves were also calculated and are presented in Fig. 7(c and d) and Fig. S7 (SI), and Fig. S8 (SI). Remarkably, all CV curves exhibit similar peaks, albeit with a corresponding offset. The proportion of pseudocapacitive and diffusive contributions was determined using eqn (6), where i represents the current, ν denotes the scan rate, $i_p = k_1\nu$ corresponds to the current associated with pseudocapacitive processes, and $i_d = k_2\nu^{0.5}$ represents the current related to diffusive processes.[46,48]

$$i(V) = k_1\nu + k_1\nu^{0.5} = i_p + i_d \qquad (6)$$

In Fig. 7(c and d), the results showed that the ion diffusion contribution decreased as the scan rate changed from 0.3 mV s^{-1} to 1.2 mV s^{-1}, while the pseudo-capacitance gradually augmented. According to Yupeng Xiao *et al.*,[46] diffusion allows the electrode to store more lithium ions by the conversion reaction mostly driven by the movement of lithium ions; meanwhile, pseudo-contribution helps to stabilize the electrode, because ion absorption and lithium ion transport mainly happen on the surface, which minimize volume changes in the electrode. The kinetic results indicated that the electrochemical reaction of the FeCC-700 samples is dominated by diffusion-controlled behavior, leading to an extended cycle life. Specifically, 0.3-FeCC-700 has a diffusive contribution ratio that is always higher than that of 0.4-FeCC-700 and 74% higher at all scan rates, because of the nanostructure and bonding morphology of 0.3-FeCC-700 nanoparticles, which help shorten the travel distance between two electrodes, allowing lithium ions to move faster. These results were consistent with the results of the previously reported electrochemical performance method and indicated that the diffusive phenomenon occurred in the FeCC anodes, which substantially influenced the entire capacity and resulted in excellent cycling performances of the 0.3-FeCC-700 hybrid composite electrode.

The electrochemical results, including the GCD profiles, CV curve and EIS spectra, consistently demonstrate that the 0.3-FeCC-700 electrode possesses better redox kinetics and lower overall polarization. In the first galvanostatic charge/discharge curves, the iR_{drop} of the 0.3-FeCC-700 electrode (1.099 V) is smaller than that of 0.4-FeCC-700 (1.1359 V), confirming a lower internal resistance during cycling (Fig. S9). Similarly, the CV curves of 0.3-FeCC-700 display narrower redox peak separation, indicating faster charge-transfer and diffusion processes. These results are in good agreement with the smaller iR_{drop} values observed in the GCD curve and the improved reversibility of the redox reactions.[49] Specifically, the CV curves shown in Fig. 6(a and b) and the data summarized in Table S2 reveal that the 0.3-FeCC-700 electrode exhibits narrower redox peak separation (ΔE_p) and smaller current responses than the 0.4-FeCC-700 electrode. The smaller ΔE_p values suggest a more reversible redox behavior and enhanced charge-transfer and Li^+ diffusion kinetics.[50] Conversely, the broader ΔE_p observed for 0.4-FeCC-700 reflects higher R_3 and slower ionic transport, which can be attributed to the partial agglomeration of Fe_3O_4 NPs and the reduction of electroactive surface area caused by

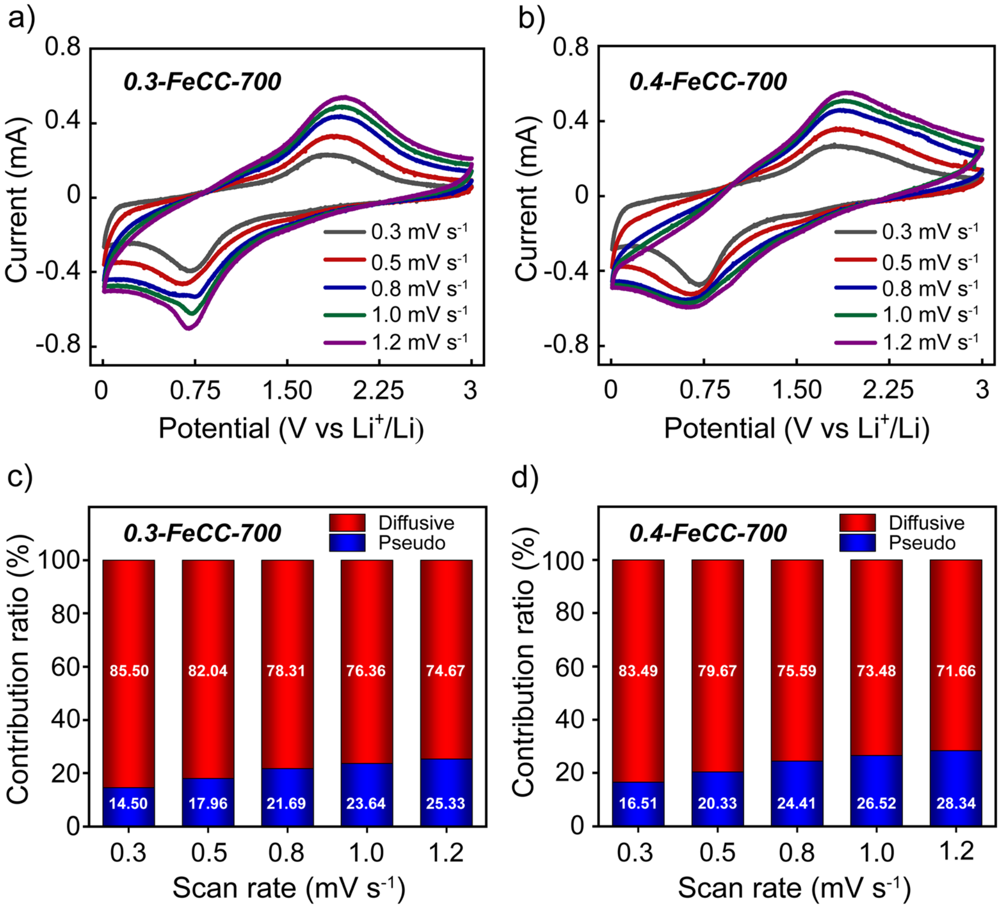

Fig. 7 (a)–(b) CV curves at various scan rates. Diffusive and pseudo-contribution plots at various scan rates for the (c) 0.3-FeCC-700 and (d) 0.4-FeCC-700 electrodes.

excessive carbonization at elevated temperatures. While the 0.4-FeCC-700 electrode showed higher R_1 and R_3 values, the 0.3-FeCC-700 sample retained a more porous and uniformly distributed nanostructure, enabling more efficient Li^+ migration and electron conduction. This structural advantage leads to faster redox kinetics and lower polarization during cycling. Therefore, both the smaller iR_{drop} in the GCD curve and the smaller ΔE_p in the CV curve confirm that the 0.3-FeCC-700 electrode exhibits lower total internal resistance and superior electrochemical reversibility, despite the slightly lower R_s difference shown in the EIS spectra. These consistent results across EIS, GCD, and CV analyses collectively validate that the 0.3-FeCC-700 electrode provides more efficient Li^+ transport pathways and better electrode kinetics than the 0.4-FeCC-700 electrode.

The crystal structure or phase component of the 0.3-FeCC-700 nanocomposite changes after the cycling test as shown in Fig. 8. The XRD patterns of the 0.3-FeCC-700 anode electrode confirm that no significant difference is observed between its fully discharged and fully charged states. However, the presence of other expected phases such as Li_2O, Li$x$$Fe_3O_4$, and Co could not be conclusively confirmed *via* XRD. Since 0.3-FeCC-700 is a novel anode material for lithium-ion batteries, its exact reaction mechanism has not yet been fully elucidated. However, we have proposed possible explanations and discussed them in the CV results, based on previous reports on partially similar materials.[2,41,42,44]

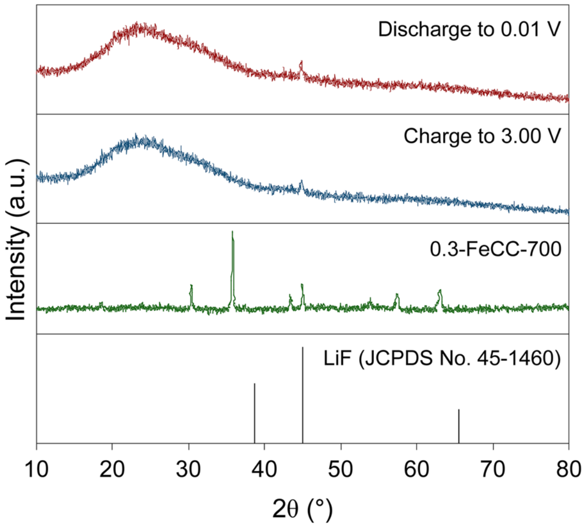

Fig. 8 *Ex situ* XRD patterns of the 0.3-FeCC-700 electrode after full discharge to 0.01 V and full charge to 3.00 V, 0.3-FeCC-700, and LiF (JCPDS No. 45-1460).

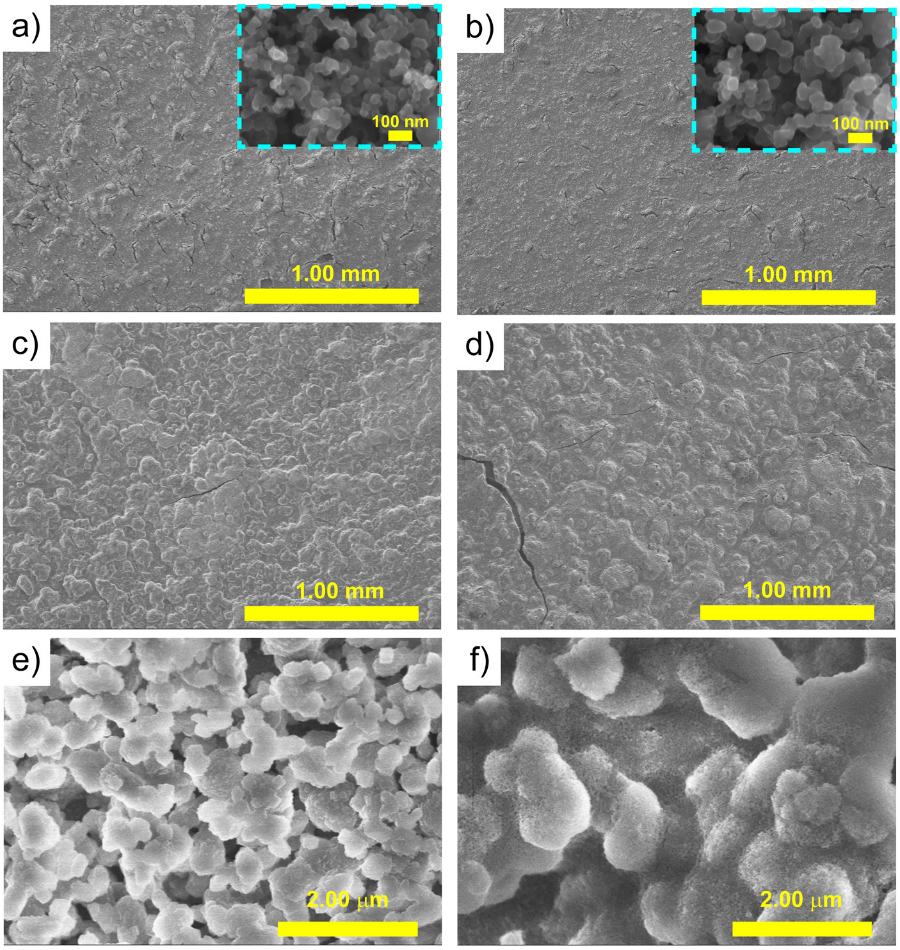

Fig. 9 *Ex situ* SEM and FESEM images of the 0.3-FeCC-700 and 0.4-FeCC-700 electrodes (a)–(b) before cycling and (c)–(d) after cycling; and the 0.3-FeCC-700 electrode when (e) discharged to 0.01 V and (f) charged to 3.00 V.

To investigate the *ex situ* structural evolution of the electrode surface and its influence on battery performance, SEM and FESEM analyses were performed on 0.3-FeCC-700 and 0.4-FeCC-700 electrodes before and after cycling. These observations reveal significant microstructural changes associated with electrochemical processes. Before cycling, both 0.3-FeCC-700 and 0.4-FeCC-700 electrodes displayed relatively uniform surfaces with well-maintained structures, although minor cracks were observed, which were likely introduced during the electrode fabrication process. As shown in the FESEM images (insets of Fig. 9(a and b)), the *x*-FeCC-700 composite exhibited a smooth nanostructured surface with no obvious surface film, indicating the absence of a pre-formed passivation layer. After 80 cycles at a current density of 0.1 A g^{-1}, notable changes in surface morphology were observed. In Fig. 9(c and d), both electrodes exhibited signs of volume expansion, a common phenomenon in conversion-type anode materials such as Fe_3O_4 NPs. However, fewer surface cracks were detected post-cycling compared to the initial state. This behavior is possibly due to the formation of a SEI film, which may have sealed surface defects and mitigated mechanical stress. Notably, the 0.4-FeCC-700 electrode exhibited more pronounced cracking and fragmentation than the 0.3-FeCC-700 electrode, suggesting that the FeCC composite in the 0.3-FeCC-700 electrode provides superior accommodation of volume changes and improved structural stability under prolonged cycling. To further assess the formation and stabilization of the SEI film, the 0.3-FeCC-700 electrode was subjected to a full lithiation/delithiation cycle (discharged to 0.01 V and charged to 3.00 V), followed by additional surface analysis in Fig. 9(e and f). Compared to the pristine electrode in the inset figure of Fig. 9(a and b), the post-cycled sample exhibited the appearance of a uniform passivation layer coating the active material particles, which is an indicator of SEI film formation. This observation was consistent with the initial discharge/charge capacity results (Fig. 5a and Fig. S5d) and the CV curve (Fig. 6a) of the 0.3-FeCC-700 anode, which indicate the formation of the SEI film at low potentials during the first cycle.

Conclusions

To summarize, we successfully fabricated FeCC hybrid composite materials derived from Fe_3O_4 nanoparticles and ZIF-67 precursors. We then evaluated the electrochemical performance of these composites as anode materials for LIBs. The results demonstrate that 0.3-FeCC-700 achieves both high capacity and stability. Specifically, this composite showed a discharge capacity of 435 mAh g^{-1} with a CE of 97% after 80 cycles. Although it has not outperformed LIB anode materials with higher reported capacities in some previous studies, the combination of Fe_3O_4 NPs and MOF-derived carbon frameworks presents an effective material engineering strategy to address capacity fading and cycling stability issues that have challenged conventional transition metal oxide anodes. The hybrid nanostructure stabilizes Fe_3O_4 NPs during lithiation/delithiation cycling, mitigating the capacity degradation typically observed in pure Fe_3O_4 nanoparticles. Additionally, the formation of composites with MOF-derived carbon overcomes the conductivity limitations of Fe_3O_4. Notably, optimizing synthesis conditions and nanostructure composition could further enhance performance. Therefore, while additional research is needed, the hybrid nanostructured FeCC materials show great promise as a foundational design for the development of high-capacity and stable LIB anodes. We propose this modular approach, as it enables the incorporation of other metal oxides and MOF precursors to further improve performance.

Author contributions

Do Thao Anh: conceptualization, data curation, formal analysis, methodology, software, writing – original draft; Nguyen Bao Tran: data curation, formal analysis, methodology; Quang Ngoc Tran: conceptualization, data curation; Hanh Kieu Thi Ta: methodology, validation; Bach Thang Phan: formal analysis, methodology, validation; Tuan Loi Nguyen: data curation, formal analysis, methodology; Nhu Hoa Thi Tran: data curation, formal analysis, funding acquisition, resources, supervision, writing – original draft, writing – review and editing.

Conflicts of interest

There are no conflicts to declare.

Data availability

The data supporting this article have been included as part of the supplementary information (SI). Supplementary information is available. See DOI: **https://doi.org/10.1039/d5ma00782h**.

Acknowledgements

This work was financially supported by Vietnam National University Ho Chi Minh City (NCM2024-50-01). We would like to gratefully acknowledge the Center for Innovative Materials and Architectures (Laboratory for Optics and Sensing) at Vietnam National University in the Ho Chi Minh City.

Notes and references

1 J. Zhao, Z. Li, S. Yao, C. Hu, J. Wang and X. Feng, Zn/Co-ZIF-derived bi-metal embedded N-doped porous carbon as anodes for lithium-ion batteries, *J. Mater. Sci.: Mater. Electron.*, 2020, **31**, 13889–13898.

2 M. Ershadi, M. Javanbakht, D. Brandell, S. Ahmad Mozaffari and A. Molaei Aghdam, Facile Synthesis of Amino-functionalized Mesoporous Fe_3O_4/rGO 3D Nanocomposite by Diamine compounds as Li-ion Battery Anodes, *Appl. Surf. Sci.*, 2022, **601**, 154120.

3 J. B. Goodenough and K. S. Park, The Li-ion rechargeable battery: A perspective, *J. Am. Chem. Soc.*, 2013, **135**, 1167–1176.

4 J. Huang, Z. Wei, J. Liao, W. Ni, C. Wang and J. Ma, Molybdenum and tungsten chalcogenides for lithium/sodium-ion batteries: Beyond MoS_2, *J. Energy Chem.*, 2019, **33**, 100–124.

5 F. Shi, Q. Liu, Z. Jin, G. Huang, B. Xing and J. Jia, *et al.*, A facile method to prepare Fe_3O_4@CTP QDs composite as advanced anode material for lithium ion batteries, *J. Alloys Compd.*, 2022, **890**, 161911.

6 K. Li, R. Qin, Y. Q. Xiong, L. Ding, J. W. Wen and M. Zeng, MOF-Derived Octahedral-Shaped Fe_3O_4@C Composites for Lithium Storage, *J. Electron. Mater.*, 2023, **52**, 3311–3320.

7 Z. Li, X. Hu, B. Li, X. Wang, Z. Shi and J. Lu, *et al.*, MOF-derived Fe_3O_4 hierarchical nanocomposites encapsulated by carbon shells as high-performance anodes for Li-storage systems, *J. Alloys Compd.*, 2021, **875**, 159906.

8 Z. Zhao, A. R. Akbar, Z. Liu, Y. Lu, Y. Chen and C. Xiong, Nondestructive CNT chained Fe_3O_4 anode materials for high-performance Li-ion batteries, *Colloids Surf., A*, 2022, **635**, 128084.

9 M. Y. Zhao, F. M. Liu, M. Chen, X. Zhang, X. Qian and Z. Y. Yuan, *et al.*, Controlled Synthesis of Fe_3N Sandwiched in Nitrogen-Doped Multilayer Graphene as an Anode Material for Lithium-Ion Batteries, *ACS Appl. Energy Mater.*, 2025, **8**, 12769–12779.

10 M. Chen, F. M. Liu, S. S. Chen, R. Wan, X. Qian and Z. Y. Yuan, Cactus-like iron oxide/carbon porous microspheres lodged in nitrogen-doped carbon nanotubes as anodic electrode materials of lithium ion batteries, *New J. Chem.*, 2023, **47**, 765–771.

11 C. Duan, Y. Yu and H. Hu, Recent progress on synthesis of ZIF-67-based materials and their application to heterogeneous catalysis, *Green Energy Environ.*, 2022, **7**, 3–15.

12 D. D. Tuan and K. Y. A. Lin, ZIF-67-derived Co_3O_4 rhombic dodecahedron as an efficient non-noble-metal catalyst for hydrogen generation from borohydride hydrolysis, *J. Taiwan Inst. Chem. Eng.*, 2018, **91**, 274–280.

13 M. Wang, F. Xi, S. Li, W. Ma, X. Wan and Z. Tong, *et al.*, ZIF-67-derived porous nitrogen-doped carbon shell encapsulates photovoltaic silicon cutting waste as anode in high-performance lithium-ion batteries, *J. Electroanal. Chem.*, 2023, **931**, 117210.

14 J. Shao, Z. Wan, H. Liu, H. Zheng, T. Gao and M. Shen, *et al.*, Metal organic frameworks-derived Co_3O_4 hollow dodecahedrons

with controllable interiors as outstanding anodes for Li storage, *J. Mater. Chem. A*, 2014, **2**, 12194–12200.

15 M. Guo, T. Gao, H. Ma and H. Li, Weaving ZIF-67 by employing carbon nanotubes to constitute hybrid anode for lithium ions battery, *Mater. Lett.*, 2018, **212**, 143–146.

16 J. Liu, J. Liang, C. Wang and J. Ma, Electrospun CoSe@N-doped carbon nanofibers with highly capacitive Li storage, *J. Energy Chem.*, 2019, 160–166.

17 Tseng P. Sen, L. X. Chang, Y. S. Ou, C. M. Chou, C. S. Tsao and Y. Wu, *et al.*, ZIF-67 derived Co nanoparticles on ZIF-Derived carbon for hydrogen spillover and storage, *Appl. Surf. Sci.*, 2023, **638**, 158097.

18 S. Frank, M. Folkjær, M. L. N. Nielsen, M. J. Marks, H. S. Jeppesen and M. Ceccato, *et al.*, Correlating the structural transformation and properties of ZIF-67 during pyrolysis, towards electrocatalytic oxygen evolution, *J. Mater. Chem. A*, 2024, **12**, 781–794.

19 L. G. Phuc, P. Q. T. Do, H. K. T. Ta, V. Q. Dang, S. W. Joo and D. H. Manh, *et al.*, Metal-Enhanced Fluorescence for Alpha-Fetoprotein Detection and for SERS Using Hybrid Nanoparticles of Magnetic Cluster Core—Plasmonic Shell Composite, *Chemosensors*, 2023, **11**, 56.

20 M. Chen, N. Wang, X. Wang, Y. Zhou and L. Zhu, Enhanced degradation of tetrabromobisphenol A by magnetic Fe_3O_4@ZIF-67 composites as a heterogeneous Fenton-like catalyst, *Chem. Eng. J.*, 2021, **413**, 127539.

21 R. K. Devi, G. Muthusankar, S. M. Chen and G. Gopalakrishnan, In situ formation of Co_3O_4 nanoparticles embedded N-doped porous carbon nanocomposite: a robust material for electrocatalytic detection of anticancer drug flutamide and supercapacitor application, *Microchim. Acta*, 2021, **188**, 1–15.

22 M. Weihai, D. Xiaomei, W. Congya, L. Yanan, W. Kai and H. Shaoliang, *et al.*, Co/C broad band electromagnetic wave absorption composite derived from preferred precursor ZIF-67: preparation and performance, *J. Mater. Sci.: Mater. Electron.*, 2020, **31**, 6418–6434.

23 L. Nyaba, T. S. Munonde, A. Mpupa and P. N. Nomngongo, Magnetic Fe_3O_4@Mg/Al-layered double hydroxide adsorbent for preconcentration of trace metals in water matrices, *Sci. Rep.*, 2021, **11**, 1–15.

24 Y. Hu, X. Song, Q. Zheng, J. Wang and J. Pei, Zeolitic imidazolate framework-67 for shape stabilization and enhanced thermal stability of paraffin-based phase change materials, *RSC Adv.*, 2019, **9**, 9962–9967.

25 S. Barsiwal, A. Babu, U. K. Khanapuram, S. Potu, N. Madathil and R. K. Rajaboina, *et al.*, ZIF-67-Metal–Organic-Framework-Based Triboelectric Nanogenerator for Self-Powered Devices, *Nanoenergy Adv.*, 2022, **2**, 291–302.

26 C. Jiang and B. Wen, Electromagnetic wave absorption performance and mechanism of Co/C composites derived from different cobalt source ZIF-67: a comparative study, *J. Mater. Sci.: Mater. Electron.*, 2022, **33**, 5730–5749.

27 M. Shahsavari, M. Mortazavi, S. Tajik, I. Sheikhshoaie and H. Beitollahi, Synthesis and Characterization of GO/ZIF-67 Nanocomposite: Investigation of Catalytic Activity for the Determination of Epinine in the Presence of Dobutamine, *Micromachines*, 2022, **13**, 88.

28 S. Zhang, Y. Zhao, Q. Yin, J. Zhang, K. J. Wang and J. Han, Hollow ZIF-67-C/LDO core/shell heterostructure as a high-performance anode material for sodium ion batteries, *Mater. Lett.*, 2021, **294**, 129817.

29 G. Gökçeli, S. Bozoğlu and N. Karatepe, Cobalt-molybdenum bimetallic catalyst effect on biomass-derived graphitic carbon, *J. Anal. Appl. Pyrolysis*, 2023, **174**, 106152.

30 A. K. Sahoo, S. Sangita Nanda, P. Nayak and S. Dash, Structural, magnetic and optical properties of Fe_3O_4@-NaGdF4 core-shell composite, *Mater. Today: Proc.*, 2023, **91**, 167–171.

31 Y. Zeng, T. Li, J. Zhong, H. Mao, M. Fu and D. Ye, *et al.*, Unraveling the role of Co_3O_4 facet for photothermal catalytic oxidation of methanol via operando spectroscopy and theoretical investigation, *J. Colloid Interface Sci.*, 2023, **643**, 360–372.

32 M. Li, D. Gao, S. Cui, Y. Shi and N. Liu, Fabrication of Fe_3O_4/ZIF-67 composite for removal of direct blue 80 from water, *Water Environ. Res.*, 2020, **92**, 740–748.

33 Y. Yan, X. Lu, Y. Li, J. Song, Q. Tian and L. Yang, *et al.*, Dispersive Fe_3O_4 encapsulated in porous carbon for high capacity and long life anode of lithium-ion batteries, *J. Alloys Compd.*, 2022, **899**, 163342.

34 X. He, Y. He, C. Wang, B. Zhu, A. Liu and H. Tang, Oxygen vacancy-rich Fe_3O_4 nanoparticle synthesized via facile electrochemical method as anode material for high-performance lithium-ion batteries, *J. Phys. Chem. Solids*, 2022, **171**, 111028.

35 X. M. Yue, Z. J. Liu, C. C. Xiao, M. Ye, Z. P. Ge and C. Peng, *et al.*, Synthesis of Co_3O_4/reduced graphene oxide by one step-hydrothermal and calcination method for high-performance supercapacitors, *Ionics*, 2021, **27**, 339–349.

36 C. Li, Y. Meng, S. Yang and H. Li, ZIF-67 Derived Co/NC Nanoparticles Enable Catalytic Leuckart-type Reductive Amination of Bio-based Carbonyls to N-Formyl Compounds, *ChemCatChem*, 2021, **13**, 5166–5177.

37 M. Xiao, Y. Meng, C. Duan, F. Zhu and Y. Zhang, Ionic liquid derived Co_3O_4/Nitrogen doped carbon composite as anode of lithium ion batteries with enhanced rate performance and cycle stability, *J. Mater. Sci.: Mater. Electron.*, 2019, **30**, 6148–6156.

38 M. Zhong, L. Kong, N. Li, Y. Y. Liu, J. Zhu and X. H. Bu, Synthesis of MOF-derived nanostructures and their applications as anodes in lithium and sodium ion batteries, *Coord. Chem. Rev.*, 2019, **388**, 172–201.

39 L. Wang, X. Bai, B. Wen, Z. Du and Y. Lin, Honeycomb-like Co/C composites derived from hierarchically nanoporous ZIF-67 as a lightweight and highly efficient microwave absorber, *Composites, Part B*, 2019, **166**, 464–471.

40 A. B. A. Abdellatif, H. M. El-Bery, H. N. Abdelhamid and S. A. El-Gyar, ZIF-67 and Cobalt-based@heteroatom–doped carbon nanomaterials for hydrogen production and dyes removal via adsorption and catalytic degradation, *J. Environ. Chem. Eng.*, 2022, **10**, 108848.

41 X. Yu, J. Yang, Z. Yuan, L. Guo, Z. Sui and M. Wang, Binder-free 3D porous Fe_3O_4–Fe2P–Fe@C films as high-performance anode materials for lithium-ion batteries, *Ceram. Int.*, 2020, **46**, 17469–17477.

42 D. Saikia, J. R. Deka, Y. C. Chen, T. C. Chuang, H. M. Kao and Y. C. Yang, CoO nanoparticles anchored on porous pinecone-derived activated carbon as anodes for high-performance lithium and sodium-ion batteries, *Ceram. Int.*, 2024, **51**, 22498–22510.

43 A. González-Banciella, D. Martinez-Diaz, J. de Prado, M. V. Utrilla, M. Sánchez and A. Ureña, MOF-derived α-Fe_2O_3@Fe_3O_4 on carbon fiber fabric for lithium-ion anode applications, *J. Energy Storage*, 2024, **90**, 111904.

44 L. Chen, B. Tang, H. Li, B. Wang and B. Huang, Porous SnO_2/Co_3O_4 nanocubes anchored onto reduced graphene oxide as a high-performance anode for lithium-ion batteries, *Solid State Ionics*, 2023, **396**, 116241.

45 J. Chen, P. F. Wang, Y. H. Zhang, D. X. Yang, X. Li and F. N. Shi, Rapid construction of surface CuO-rich Co_3O_4/CuO composites as anodes for high-performance lithium-ion batteries, *J. Solid State Chem.*, 2023, **318**, 123787.

46 Y. Xiao, T. Li, Y. Mao, X. Hao, W. Wang and S. Meng, *et al.*, Core-shell N-doped carbon embedded Co_3O_4 nanoparticles with interconnected and hierarchical porous structure as superior anode materials for lithium-ion batteries, *J. Energy Storage*, 2023, **63**, 106998.

47 A. C. Lazanas and M. I. Prodromidis, Electrochemical Impedance Spectroscopy—A Tutorial, *ACS Meas. Sci. Au*, 2023, **3**, 162–193.

48 C. Yue, D. He, X. Zeng, Z. Ma, L. He and Z. Meng, *et al.*, Freestanding hybrid electrospun membranes consisting of TiO_2 nanotube-core nanocarbon as high-performance and long-lifespan anodes for lithium-ion batteries, *J. Alloys Compd.*, 2023, **961**, 171026.

49 C. Liu, Z. G. Neale and G. Cao, Understanding electrochemical potentials of cathode materials in rechargeable batteries, *Mater. Today*, 2016, **19**, 109–123.

50 R. Wang, S. Boyd, P. V. Bonnesen and V. Augustyn, Effect of water in a non-aqueous electrolyte on electrochemical Mg^{2+} insertion into WO_3, *J. Power Sources*, 2020, **477**, 229015.